Generation of remote adaptive torsional shear waves with an octagonal phased array to enhance displacements and reduce variability of shear wave speeds: comparison with quasi-plane shear wavefronts

Abderrahmane Ouared[1,2], Emmanuel Montagnon[1,2,4] and Guy Cloutier[1,2,3,5]

[1] Laboratory of Biorheology and Medical Ultrasonics, University of Montréal Hospital Research Center (CRCHUM), Montréal, QC, Canada
[2] Institute of Biomedical Engineering, University of Montréal, Montréal, QC, Canada
[3] Department of Radiology, Radio-Oncology and Nuclear Medicine, University of Montréal, Montréal, QC, Canada

E-mail: guy.cloutier@umontreal.ca

Abstract

A method based on adaptive torsional shear waves (ATSW) is proposed to overcome the strong attenuation of shear waves generated by a radiation force in dynamic elastography. During the inward propagation of ATSW, the magnitude of displacements is enhanced due to the convergence of shear waves and constructive interferences. The proposed method consists in generating ATSW fields from the combination of quasi-plane shear wavefronts by considering a linear superposition of displacement maps. Adaptive torsional shear waves were experimentally generated in homogeneous and heterogeneous tissue mimicking phantoms, and compared to quasi-plane shear wave propagations. Results demonstrated that displacement magnitudes by ATSW could be up to 3 times higher than those obtained with quasi-plane shear waves, that the variability of shear wave speeds was reduced, and that the signal-to-noise ratio of displacements was improved. It was also observed that ATSW could cause mechanical inclusions to resonate in heterogeneous phantoms, which further increased the displacement contrast between the inclusion and the surrounding

[4] Present address: Rheolution Inc., Montréal, QC, Canada.
[5] Author to whom any correspondence should be addressed.

medium. This method opens a way for the development of new noninvasive tissue characterization strategies based on ATSW in the framework of our previously reported shear wave induced resonance elastography (SWIRE) method proposed for breast cancer diagnosis.

(Some figures may appear in colour only in the online journal)

1. Introduction

Remote excitation techniques use acoustic radiation force to generate shear waves in dynamic elastography (Rudenko *et al* 1996, Sarvazyan *et al* 1998, 2010). This strategy posed the framework of acoustic radiation force impulse (ARFI) imaging, which combines dedicated beamforming to remotely induce shear waves and imaging sequences for subsequent tracking (Nightingale *et al* 2001, 2002, 2003). Supersonic shear imaging (SSI), on the other hand, allows multipoint focalization of a radiation pressure at different depths on the same axial line to produce quasi-plane shear wavefronts (Bercoff *et al* 2004). Constructive interferences between each source generated at different depths create wavefronts with greater magnitudes (Bercoff *et al* 2004). Remote dynamic ultrasound elastography methods implemented on commercial scanners, such as ARFI and SSI, mainly rely on estimating elasticity of the probed medium by tracking the shear wave velocity, which is related to the tissue elasticity through $E \approx 3\ \mu$ and $\mu = \rho v_s^2$ (E: Young's modulus, μ: shear modulus, ρ: density and v_s: velocity of propagating shear waves). In some other techniques (Chen *et al* 2013a, 2013b), viscoelasticity could be assessed by estimating the shear wave velocity at different frequencies and by fitting the data to a basic rheological model. Another approach (Montagnon *et al* 2014) consisted in estimating viscoelastic properties through the solution of an inverse shear wave propagation problem using analytical modeling or the finite element method (FEM).

However, one problem of dynamic elastography techniques using remote palpation (i.e. an acoustic radiation force) is the strong attenuation of shear waves with the propagation distance (Palmeri *et al* 2008, Deffieux *et al* 2009). This attenuation can be related to the type of shear waves generated (i.e. circular, quasi-planar, etc...) and to the properties of the propagation medium (i.e. viscosity, dispersion and scattering). On a few millimeters, the amplitude and signal-to-noise ratio (SNR) of estimated displacements considerably decrease. This causes the tracking of shear waves and estimation of shear moduli difficult or even impossible, which affects biological tissue characterization (Deffieux *et al* 2009). Note that the same observation applies to viscosity estimates where good displacement SNR is also necessary for optimum assessment (Montagnon *et al* 2014).

As the amplitude of the induced displacement field depends on the deposited energy produced by the radiation force (Nightingale *et al* 2001), one strategy to counterbalance the effect of tissue attenuation is to enhance the intensity of the radiation pressure. This may be achieved by increasing the push duration and/or the excitation amplitude of the transducer (Calle *et al* 2005, Elkateb Hachemi *et al* 2006). This approach, however, is limitative due to food and drug administration (FDA) thresholds imposed for *in vivo* applications (Barnett *et al* 2000), and because of safety limits to assure the integrity of transducer elements. In Tanter *et al* (2008) and Song *et al* (2012), it was proposed to repeat the data acquisition with different push beam locations to compensate the attenuation. Another strategy was to adapt the excitation

frequency of the radiation source to optimize its intensity (Ouared *et al* 2015). Optimizing the radiation force to compensate for the attenuation of biological tissues is still a timely issue.

The present study is inspired by the work of Ekeom *et al* (2013). In the latter report, an adaptive torsional shear wave (ATSW) method was proposed to amplify tissue displacements and to promote mechanical resonance in the case of a heterogeneous medium containing an inclusion, such as a breast lesion. The concept of using torsional shear waves to induce a mechanical resonance and an amplification of tissue displacements was recently proven *in vivo* in a volunteer with a breast fibroadenoma (Hadj-Henni *et al* 2012). In this study, an oscillating cup applied on the surface of the woman breast was used to induce polarized torsional waves. In the current study, various strategies for the generation of ATSWs with a mimicked octagonal transducer array were investigated to enhance tissue displacements, shear wave velocity accuracy, and the SNR. The proposed method was tested on viscoelastic homogeneous and heterogeneous phantoms containing soft and hard inclusions. Data processing was performed in the temporal and frequency domains to determine resonance frequencies of mechanical heterogeneities and to assess the increase in displacements at specific frequencies. The amplitude of displacements obtained with the ATSW method reached 3.5 times those generated by quasi-plane shear waves.

2. Materials and methods

The theoretical concept of an octagonal phased array consisting of 8 linear segments of transducers with 256 elements each (total of 2048 elements) was recently introduced by our team to generate ATSWs (Ekeom *et al* 2013). To mimic this octagonal probe, an experimental prototype was made using a linear array transducer with 128 elements (ATL L7-4, Philips, Bothell, WA, USA) controlled by an ultrasound research scanner (model V1, Verasonics Inc., Redmond, WA, USA). Several quasi-plane shear wavefronts were generated iteratively and combined in post-processing using a reconstruction algorithm. The accuracy of the reconstruction method was evaluated with FEM simulations. Figure 1 illustrates the whole experimentation protocol.

2.1. Adaptive torsional shear waves

Torsional waves can be generated by combining several quasi-plane shear wavefronts around a closed path (figure 2). During their inward propagation, these wavefronts are combined and generate interferences (see figure 9 of Ekeom *et al* (2013) for a theoretical description). The amplitude of displacements with such strategy can be enhanced by constructive interferences. Due to the small amplitude of shear wave induced displacements, we assumed linear acoustic conditions to describe the propagation of shear waves. In this case, if U_1 and U_2 are the displacements induced by shear wave fields S_1 and S_2, respectively, then $U_1 + U_2$ can be considered as the total displacement induced by the shear wave field $S_1 + S_2$ (superposition principle) (Fink 1992). Thus, to mimic the generation of ATSWs according to the theoretical concept of the octagonal probe of Ekeom *et al* (2013) and the frequency adaptation method of Ouared *et al* (2015), eight quasi-plane shear wavefronts were generated separately and combined linearly in post-processing, as in Hah *et al* (2012) and Hazard *et al* (2012) for the case of the crawling wave dynamic elastography method.

2.2. Ultrasound transducer characterization

To assure that FDA thresholds for *in vivo* medical ultrasound applications are not exceeded (Barnett *et al* 2000), we experimentally determined the maximum intensity (I_{SPPA}), the time
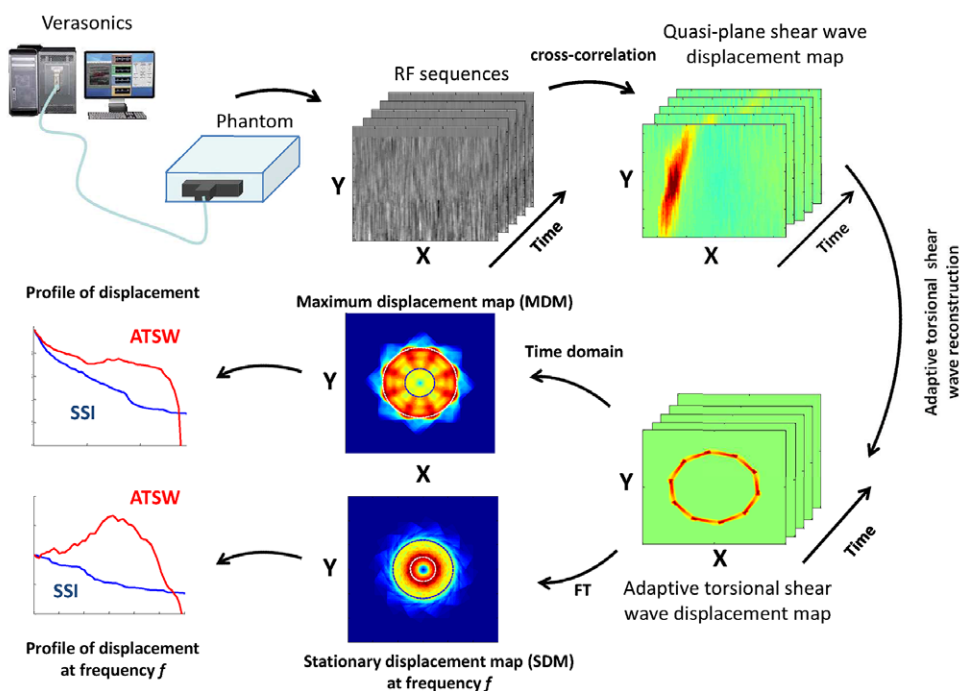
Figure 1. Schematic illustration of the experimental setup and data post-processing.
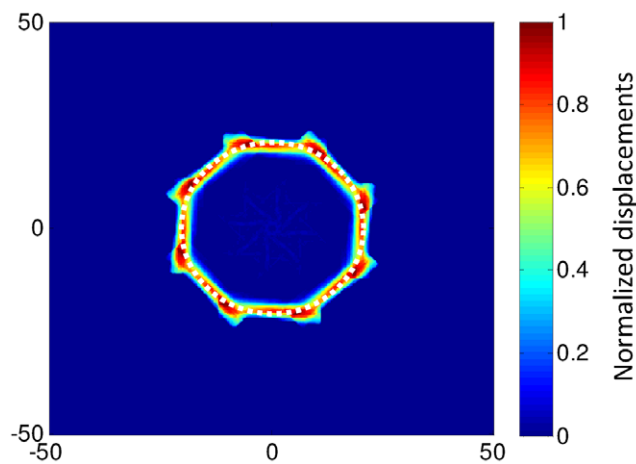

Figure 2. Schematic illustration of the combination of the eight quasi-plane wavefronts around a closed path (dashed white circle) to generate the adaptive torsional shear wave (ATSW). The color scale from blue (minimum), green and red (maximum) indicates the amplitude of normalized displacements. *X* and *Y* distances are in mm.

average intensity (I_{SPTA}) and the mechanical index (MI) (Acevedo and Das-Gupta 2002) of the acoustic parameters used in this study. As mentioned previously, the transducer used in the whole experimentation protocol was an ATL L7-4 (central frequency $f_c = 5$ MHz, bandwidth at full width half maximum $= 3.5$ MHz, and the pitch was 0.308 mm). The excitation
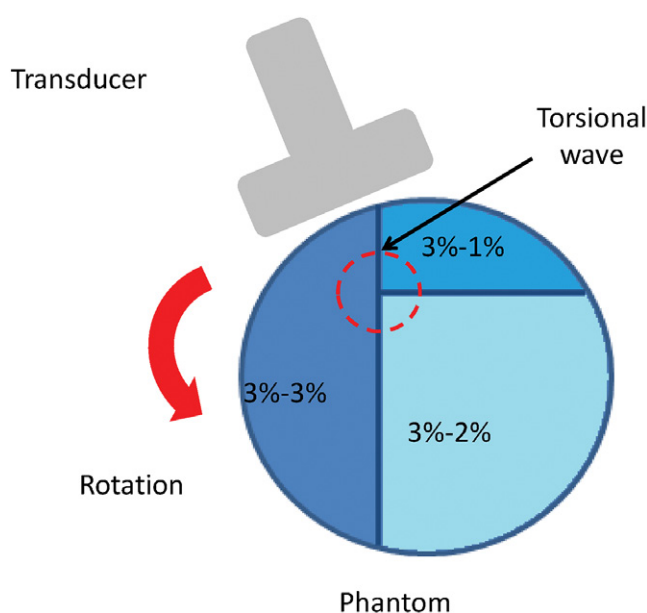
Figure 3. Schematic representation of the complex heterogeneous phantom #6. Torsional shear waves were generated around an eccentric closed circular path by moving the position of the transducer. Percentages represent proportions of agar and gelatin.

amplitude (transducer voltage) used to generate the radiation force was fixed at 30 volts. The radiation force was created at 5 MHz and focused for these specific measurements at 30 mm in degassed water at room temperature (23.2 °C). The burst duration of the excitation sequence was 100 μs. See Ouared *et al* (2015) for details on the protocol used to measure I_{SPPA}, I_{SPTA} and MI with a hydrophone. See the appendix for equations considered for those calculations.

2.3. Fabrication of phantoms and determination of their shear moduli

Six biological tissue mimicking phantoms with different mechanical properties were fabricated to assess the performance of the ATSW method. They consisted in three homogenous blocks of gel (phantoms #1, #2 and #3) and three heterogeneous ones (phantoms #4, #5 and #6). Phantoms #4 and #5 were constituted of a surrounding medium with a cylindrical inclusion at its center (radius of inclusions = 5 mm), and phantom #6 was made of three different parts (figure 3). All phantoms had the same volume (1000 cm^3) and were made with agar (product N° A-9799, Sigma–Aldrich Chemical, St Louis, Mo, USA) and gelatin (product N° G-2500, Sigma–Aldrich Chemical) mixtures with different concentrations following the protocol described in Gennisson and Cloutier (2006). Samples were taken from each gel mixture used to fabricate surrounding media, inclusions and the complex phantom #6 to estimate their shear moduli according to the time of flight algorithm applied on propagating shear waves, using the method of Bercoff *et al* (2004). Table 1 summarizes details on concentrations used for the preparation of each phantom and their corresponding shear moduli. Percentages are in proportion of the water weight.

Table 1. Concentrations of agar and gelatin used for fabricating each phantom and their corresponding shear moduli. Proportions are relative to the water weight.

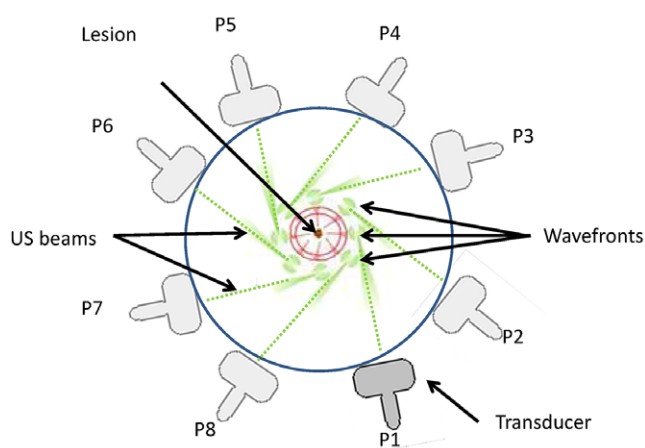| Phantoms		#1	#2	#3	#4	#5	#6
Concentration	Surrounding (agar—gelatin)	2%–3%	3%–4%	4%–5%	3%–4%	3%–4%	N/A
	Inclusion (agar—gelatin)	N/A	N/A	N/A	2%–3%	4%–5%	N/A
	Complex medium (agar—gelatin)	N/A	N/A	N/A	N/A	N/A	3%–3%
							2%–3%
							1%–3%
Elasticity	Surrounding	2.1 ± 0.3 kPa	7.2 ± 0.43 kPa	12.5 ± 0.36 kPa	7.2 ± 0.43 kPa	7.2 ± 0.43 kPa	N/A
	Inclusion	N/A	N/A	N/A	2.1 ± 0.43 kPa	12.5 ± 0.36 kPa	N/A
	Complex medium	N/A	N/A	N/A	N/A	N/A	1.9 ± 0.32 kPa
							1.4 ± 0.23 kPa
							0.7 ± 0.17 kPa

Figure 4. Schematic representation of the mechanical rotation of the ultrasound transducer around the phantom from position 1 (P1) to position 8 (P8).

2.4. Production of frequency-adapted quasi-plane shear waves and tracking of tissue displacements

Eight quasi-plane shear wavefronts were remotely generated at eight different positions around a circular path (figure 4). At each position, the wavefront was produced by a home-made implementation similar to the SSI technique (Mach number = 100) (Bercoff *et al* 2004), called adaptive ultrasound supersonic beam (AUSB) (Ouared *et al* 2015). Each quasi-plane wavefront was produced by three focused radiation pressure pushes 2 mm apart from each other. The focal spot size of each focus was approximately 8 mm. For each focus, we optimized the energy delivery by adapting the excitation frequency applied on the transducer by considering the theoretical model of Ouared *et al* (2015) and experimental measurements of the attenuation coefficient of the medium. The attenuation coefficient was estimated from acquired radio frequency (RF) data using the spectral shift method (Narayana and Ophir 1983, Mamou and Oelze 2013).

As used earlier for the determination of acoustic intensities, the transducer excitation voltage was fixed at 30 volts for the whole experimental protocol. The number of firing cycles at each frequency was adjusted to the closest integer to obtain a push duration of approximately 100 μs. Tracking of shear waves (imaging phase) was performed immediately after the pushing phase using the ultrafast plane wave imaging method described in (Montagnon *et al* 2014), allowing retrospective image reconstruction at a frame rate of 4000 Hz. After estimating displacements from acquired RF data using a one-dimensional (1D) normalized cross-correlation algorithm implemented on GPU (graphic processing units) (Montagnon *et al* 2012), 2D displacement images in the temporal domain were obtained, as in Hadj-Henni *et al* (2010) and Schmitt *et al* (2011). Measurements were repeated ten times and mean values and standard deviations were reported.

2.5. Reconstruction of frequency-adapted torsional shear wave patterns

As mentioned previously, the circular ATSW fields were reconstructed from quasi-plane shear wavefronts by considering the linear superposition of displacement maps. The eight

quasi-plane wavefronts, produced by the home-implemented AUSB sequence, were generated separately by moving the transducer around the phantom and combined to form a circular path (figure 2), as theoretically depicted in Ekeom *et al* (2013). The transducer was mechanically rotated around phantoms at locations P1 to P8 using a 3D positioner (figure 4). Each AUSB wavefront was considered to be generated simultaneously. Linearly superposed displacement fields accounted for all constructive and destructive shear wave interferences. The ATSW displacement field is a vector field, and as phantoms #1 to #5 were either homogeneous or constituted of an inclusion located at their center position, the different wavefront paths were similar. Therefore, there was no phase difference in the generation of the different quasi-plane wavefronts and the sum of all displacements at the center was thus zero, as illustrated in examples given below (see the results). In the case of the phantom #6, propagation paths of the different wavefronts were not similar due to the heterogeneity of the medium and absence of axis symmetry. Therefore, phases (delays) were introduced to generate the different quasi-plane wavefronts. A first sequence with a zero phase was done to characterize each propagation path, and a second sequence was fired and adjusted by introducing estimated phases to take delays into consideration.

For homogeneous phantoms (phantoms #1, #2 and #3), three circular ATSWs with different radii (R_{ATSW} = 10, 15 and 20 mm, where R_{ATSW} is the radius of the circular path) were generated. In the case of heterogeneous phantoms #4 and #5, only one circular ATSW was generated around inclusions with R_{ATSW} = 15 mm. In this case, the ATSW field and the inclusion had the same center and were assumed to be concentric. An eccentric circular path with R_{ATSW} = 20 mm was considered in the case of the complex phantom #6. From 2D ATSW displacement maps, the maximum amplitude at each pixel of the image over time was defined to produce the maximum displacement map (MDM). Stationary displacement maps (SDM) were also computed from the complex amplitude of each pixel at a specific frequency using the fast Fourier transforms (FFT), as in Hadj-Henni *et al* (2010) and Schmitt *et al* (2011, 2013) (figure 1). MDM images were normalized to its maximum displacement at the same depth as the central focused push at a lateral distance of 3.6 mm, which corresponded to the beginning of the generated wavefront (figure 5) as shear waves are not present in the push beam region (Bercoff *et al* 2004, Tanter *et al* 2008, Song *et al* 2012). In the case of SDM, each map was normalized to the amplitude of displacements at the same position as for MDM, but at the corresponding frequency analyzed.

To quantify the benefit of the ATSW strategy over AUSB, the relative displacement (RD) at a given distance from the push beam was computed as the ratio of the amplitude at that location to the amplitude at the focused push (see equation (A.4) in the appendix). The displacement SNR was also evaluated in regions of interest (ROI) defined as a rectangle of 10 mm (axially) by 3 mm (laterally), localized at the same depth as the focused push at lateral distances (from the push location) of 5, 10 and 15 mm for ATSW with R_{ATSW} = 10, 15 and 20 mm, respectively. The SNR was computed as the ratio of the mean displacement by its standard deviation (Nightingale *et al* 2002). Finally, to assess the impact of the enhancement in displacements on the shear modulus measurements, the shear wave velocity of AUSB and ATSW (with R_{ATSW} = 20 mm) methods were measured in two different ROIs of homogeneous phantoms (phantoms #1, #2 and #3), using the time-of-flight algorithm (Bercoff *et al* 2004). ROIs were defined as a rectangle of 10 mm (axially) by 5 mm (laterally), located at the same depth as the focused push and at lateral distances (from the push location) of 1 mm for the first ROI and 13 mm for the second one. For each phantom, experiments were repeated ten times and averaged results (RD, SNR and shear wave velocities) are reported.
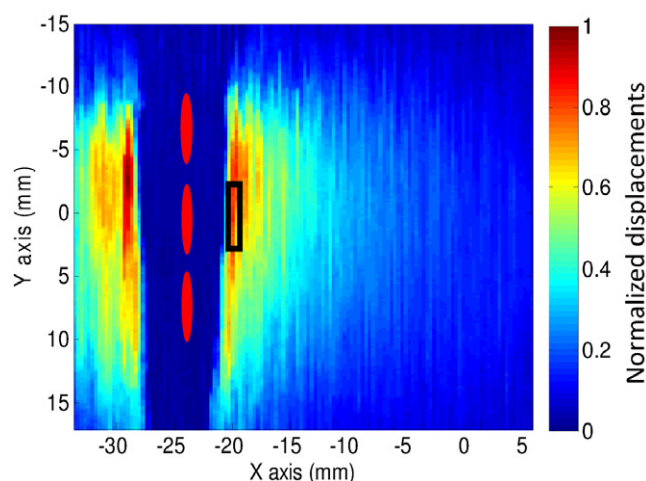
Figure 5. Example of the maximum displacement map (MDM) of a quasi-plane shear wave used in the reconstruction of the adaptive torsional shear wave strategy. The three red ellipses illustrate where focused pushes were produced. The maximum amplitude of the displacement at the same depth as the central focused push, and at a lateral distance of 3.6 mm (black rectangle), was used for the normalization. The color scale from blue (minimum), green and red (maximum) indicates the amplitude of normalized displacements.

2.6. Finite element method modeling

The aim of the FEM simulation was (1) to validate the reconstruction code and to show that displacement fields reconstructed from simulated quasi-plane shear waves were equivalent to a torsional shear wave created with focused pushes generated simultaneously around a closed path, and (2) to validate experimental results. Quasi-plane shear wave and circular adaptive torsional shear wave propagations were simulated in 2D by finite element modeling (COMSOL Inc., ver. a3.5, Burlington, MA, USA). First, eight quasi-plane shear wave fronts originating from different positions around the circular path were simulated individually. Two simulation strategies were thereafter considered. The first circular adapted torsional wavefront ($R_{ATSW} = 20$ mm) was simulated by eight focused pushes generated simultaneously in the FEM model. The second circular adaptive torsional shear wave front (same radius) was reconstructed (using the linear superposition reconstruction algorithm) from the above mentioned eight simulated quasi-plane shear wavefronts distributed around the circular path.

These different shear wave propagation patterns were generated by imposing a transient displacement (figure 6) at each node defining the region of focused pushes, which was modeled as an ellipse with long and short axis diameters of 6 and 2 mm, respectively. The propagation medium was assumed isotropic, linear, homogeneous with the same value of the shear modulus of phantom #2 ($\mu = 7.2$ kPa), which was arbitrary chosen, and modeled as a finite square region (1×1 m^2) much larger than the radius R_{ATSW} to avoid undesirable reflections at boundaries. An extra fine mesh element size was used; it was fixed at one third of a millimeter. The time step was selected at 0.1 ms, which corresponds to a frame rate of 10 kHz. All FEM simulations were performed in the time domain and consequently the viscous component was not taken into account. Displacement amplitudes were normalized relative to the amplitude of displacement at the focused push.
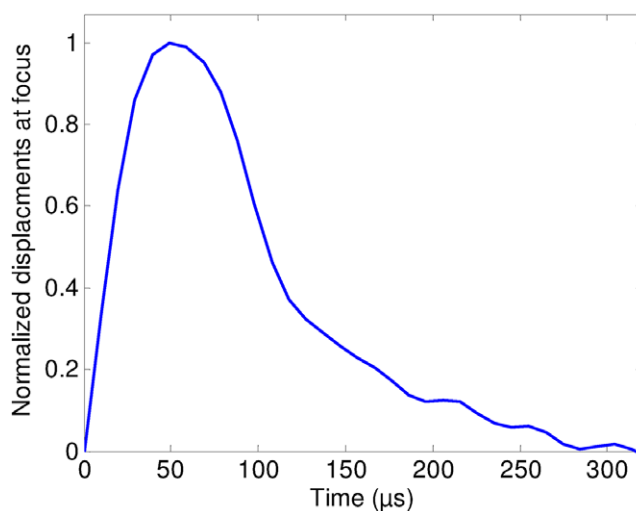
Figure 6. Normalized temporal displacement at the focus of the transient excitation.

3. Results

3.1. Validation of the reconstruction algorithm with the finite element method

Figure 7(a) shows the MDM of a simulated (FEM) quasi-plane shear wavefront, whereas figure 7(b) presents the MDM of the simulated circular adaptive torsional shear wavefront obtained by superposing eight quasi-plane shear waves generated simultaneously in a medium corresponding to phantom #2. Globally, similar patterns of displacements as panel (b) are depicted in panel (c), which represents the MDM obtained by finite element modeling of circular ATSW. Panel (d) depicts the experimentally reconstructed MDM assuming linear superposition (also for the case of phantom #2). Black arrows on this figure represent the propagation distance begging at the foremost left sided focused push location (shear wave source).

By convention, in upcoming figures, simulation results are depicted by blue lines whereas experimental data are in red. Figure 8(a) illustrates simulated displacements along the propagation distance (black arrows of figure 7). One can observe similarities between reconstructed (dashed blue) and FEM simulated (solid blue) ATSW. The correlation coefficient between these profiles of displacements was $R^2 = 0.97$, whereas mean and maximum relative errors (RE) computed with equation (A.5) in the appendix were 0.5% and 11.3%, respectively. At the opposite, the simulated quasi-plane wavefront (dotted blue) depicted a strong attenuation with distance. Figure 8(b) compares displacements along the propagation distance between simulated (dashed blue) and experimental (dashed red) ATSW reconstructed profiles. The correlation coefficient between the two profiles was $R^2 = 0.87$, the mean RE was 16.2%, and the maximum RE was 31.6%.

3.2. Safety consideration

Experimental measures of the maximum intensity (I_{SPPA}) for selected firing conditions was $96 \pm 1\,\mathrm{W.cm^{-2}}$, that of the average intensity (I_{SPTA}) was 9.6 ± 0.2 mW.cm^{-2}, and the
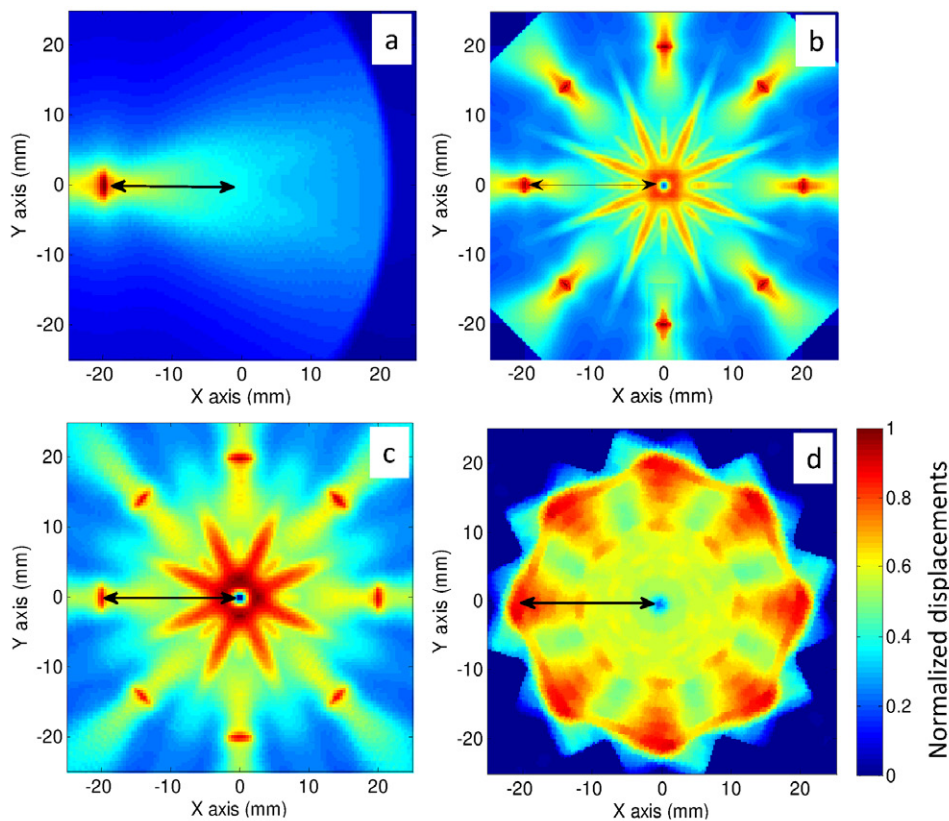
Figure 7. (a) Maximum displacement map (MDM) of simulated (FEM) quasi-plane shear wavefront (zoomed with respect to other panels), (b) MDM of reconstructed adaptive torsional shear wavefront by considering eight simulated quasi-plane shear wavefronts as in (a) around a circular path, (c) MDM of FEM simulated adaptive torsional shear wavefront, and (d) MDM of experimental adaptive torsional shear wavefront in the case of phantom #2. Black arrows represent the propagation distance begging at the shear wave source. MDM images were normalized to its maximum displacement amplitude at the same depth as the center of the focused push, at a lateral distance of 3.6 mm, which corresponded to the beginning of the propagation of the generated wavefront. The color scale from blue (minimum), green and red (maximum) indicates the amplitude of normalized displacements.

mechanical index (MI) was 0.27 ± 0.01. These values are within the acceptable range suggested by the FDA for *in vivo* applications (Barnett *et al* 2000).

3.3. Impact of frequency-adapted torsional shear waves on displacement enhancements

Figure 9 compares experimental maximum displacements (or MDM) of the quasi-plane shear wave strategy (dotted red) with ATSW (dashed red) generated at different radii ($R_{ATSW} = 10$, 15 and 20 mm) as a function of the propagation distance in homogeneous phantoms. As expected from FEM simulations (e.g. see figure 8(a)—dotted blue curve), the amplitude of quasi-plane shear waves decreased rapidly with the propagation distance, whereas after an inward propagation on a few wavelengths, the amplitude of adaptive torsional shear waves
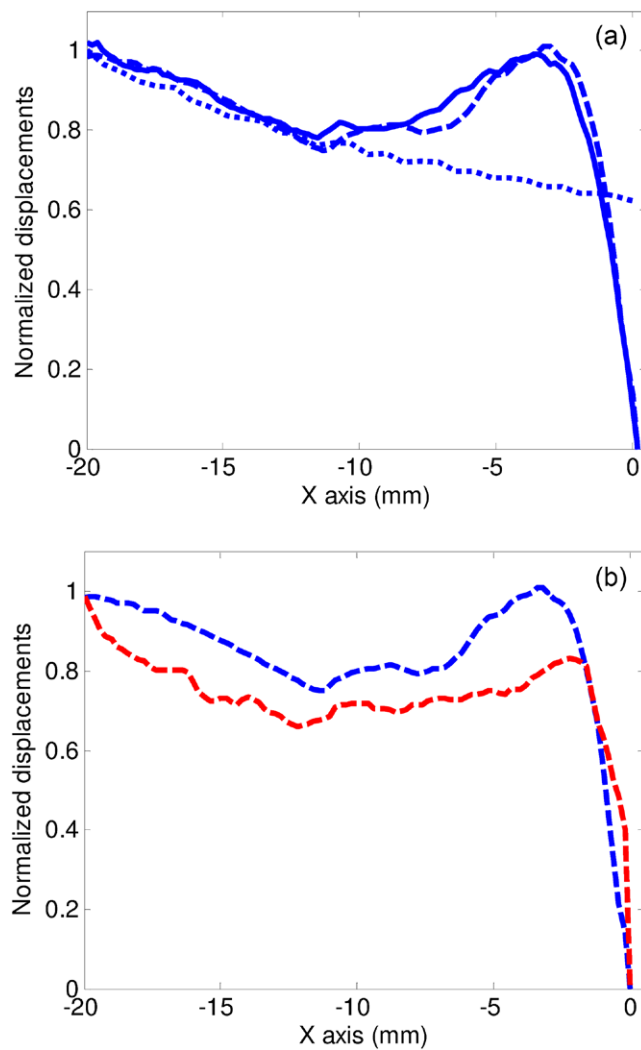
Figure 8. Normalized maximum displacement profiles along black arrows in figure 7 as a function of the traveled distance from the foremost left-sided shear wave source. (a) Comparison between displacements of the simulated quasi-plane shear wavefront corresponding to figure 7(a) (dotted blue), reconstructed simulated adaptive torsional shear wavefront of figure 7(b) (dashed blue), and FEM simulated adaptive torsional shear wavefront of figure 7(c) (solid blue). (b) Comparison between simulated (dashed blue) and experimental (dashed red) maximum displacements corresponding to figures 7(b) and (d), respectively. MDM images were normalized to its maximum displacement amplitude at the same depth as the center of the focused push, at a lateral distance of 3.6 mm, which corresponded to the beginning of the propagation of the generated wavefront.

increased with distance. Typically, in phantom #1 for $R_{ATSW} = 10$ mm (figure 9(a1)), the relative displacement (RD in equation (A.4) of the appendix) after a propagation on 9 mm was 89% of the generated push magnitude for ATSW but only 53% for the quasi-plane shear wavefront (i.e. AUSB). With $R_{ATSW} = 15$ mm (figure 9(a2)), the relative displacement after a propagation on 14 mm was 78% for ATSW and 39% for AUSB. For the same phantom with
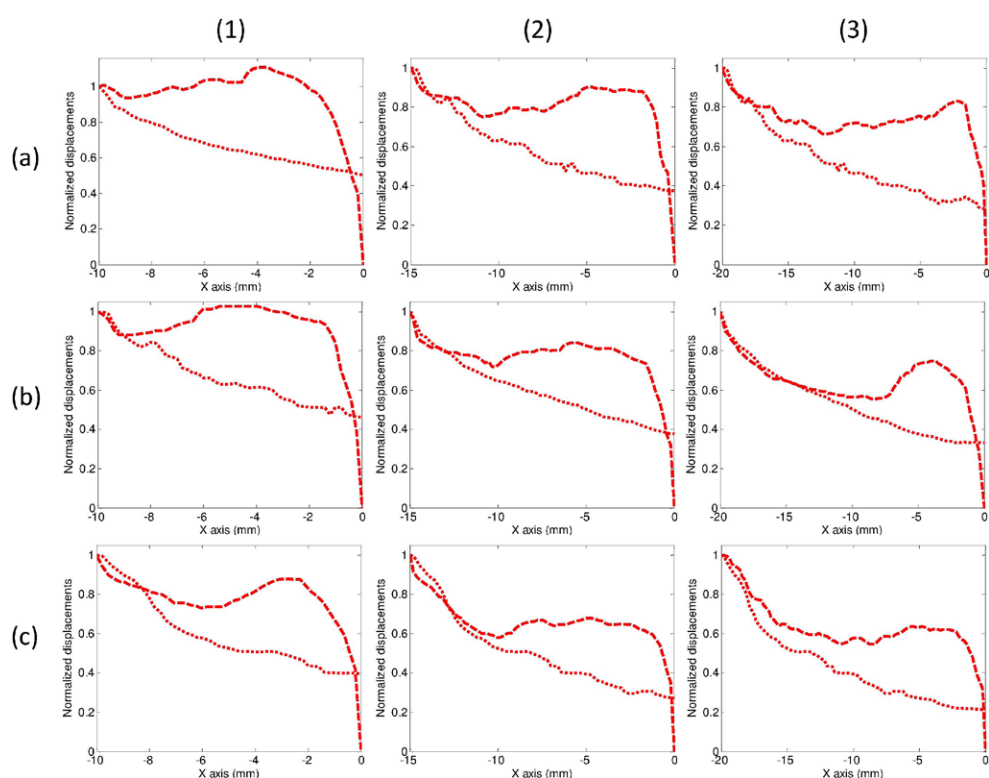
Figure 9. Experimental normalized maximum displacements as a function of the traveled distance (along black arrows in figure 7) for quasi-plane shear wavefront (dotted red) and adaptive torsional shear wavefront (dashed red) in homogeneous phantom #1 (a), phantom #2 (b) and phantom #3 (c). Columns correspond to three different radii of the circular path used to produce torsional waves: $R_{ATSW} = 10\,mm$ (1), $R_{ATSW} = 15\,mm$ (2) and $R_{ATSW} = 20\,mm$ (3). The distance of 0 mm corresponds to the center symmetry axis of the circular adaptive torsional shear wavefront. MDM images were normalized to its maximum displacement amplitude at the same depth as the center of the focused push, at a lateral distance of 3.6 mm, which corresponded to the beginning of the propagation of the generated wavefront.

$R_{ATSW} = 20\,mm$ (figure 9(a3)), the relative displacement after a propagation on 19 mm was 68% for ATSW and only 32% for AUSB. For phantoms #2 and #3 (figures 9(b) and (c)), similar behaviors are observed.

Figures 10(a) and (b) shows the MDM of ATSW within the soft heterogeneity of phantom #4, and a comparison between normalized maximum displacements of AUSB versus ATSW. Relative displacements inside the inclusion were between 19% and 39% for AUSB, whereas it varied between 0% (at the center axis) to 79% for ATSW. Figures 11(a) and (b) illustrates similar results for the case of phantom #5 with a hard inclusion. As seen in panel (b), normalized displacements decreased uniformly for AUSB until reaching the interface of the inclusion, where a sudden decay in magnitude is observed followed by another uniform decay within the inclusion. For ATSW, displacements decreased and then increased due to constructive interferences after propagating on a few millimeters. At the inclusion interface, displacements decreased before fading out at the center of the circular path. Within the hard
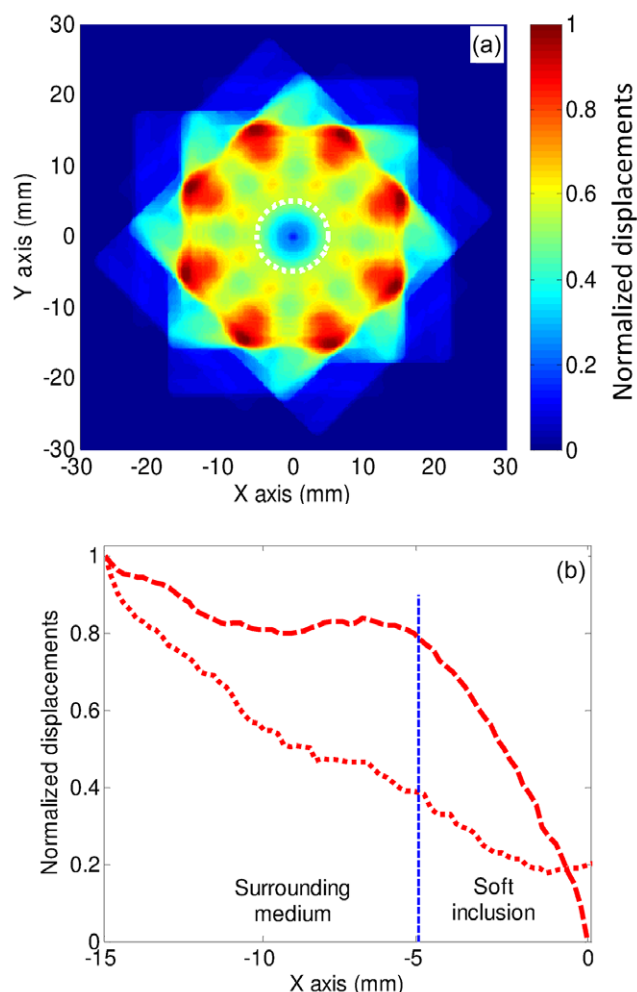
Figure 10. (a) Normalized maximum displacement map of adaptive torsional shear waves generated around the soft inclusion of phantom #4 with $R_{ATSW} = 15$ mm. The white dashed circle represents the position of the soft inclusion. The color scale from blue (minimum), green and red (maximum) indicates the amplitude of normalized displacements. (b) Comparison between displacements of quasi-plane shear waves (dotted red) and adaptive torsional shear waves (dashed red). The distance of 0 mm corresponds to the center symmetry axis of the circular adaptive torsional shear wavefront corresponding to the center of the soft inclusion. MDM images were normalized to its maximum displacement amplitude at the same depth as the center of the focused push, at a lateral distance of 3.6 mm, which corresponded to the beginning of the propagation of the generated wavefront. The vertical dashed blue line represents the interface between the surrounding medium and the soft inclusion.

inclusion, displacements remained up to 72% of the initial amplitude for ATSW, whereas it was less than 41% for the quasi-plane shear wavefront.

Figures 12(a) and (b) illustrates the MDM of ATSW generated in phantom #6 with zero phases and adjusted phase delays, respectively. Figure 12(c) shows normalized displacements of the adaptive torsional shear wave strategy generated with zero phases (dashed-dotted red),
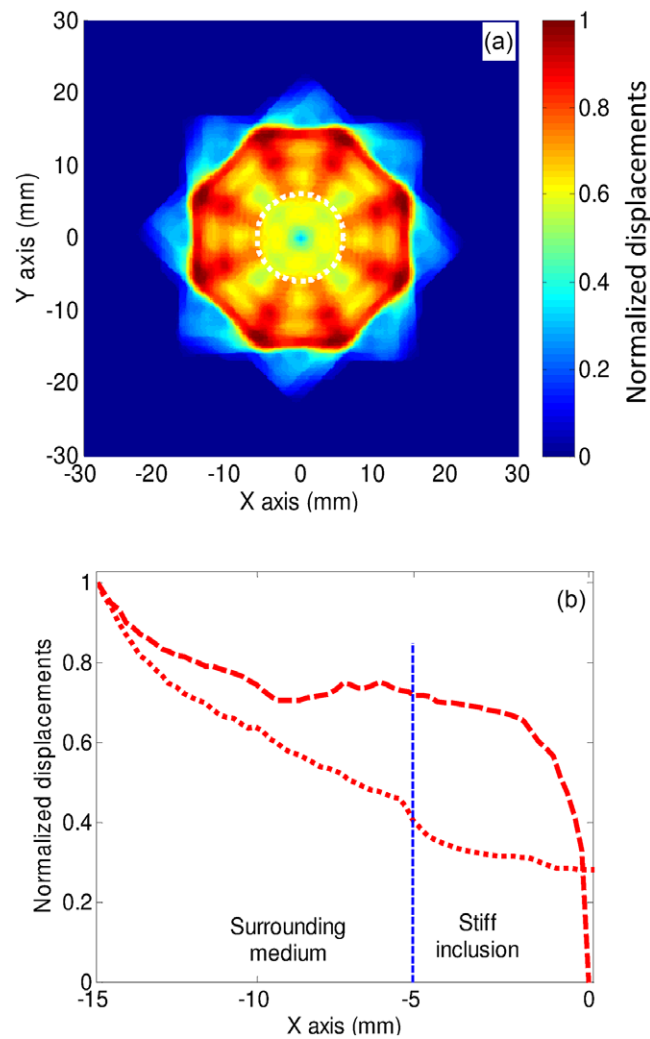
Figure 11. (a) Normalized maximum displacement map of adaptive torsional shear waves generated around the hard inclusion of phantom #5 with $R_{ATSW} = 15$ mm. The white dashed circle represents the position of the hard inclusion. The color scale from blue (minimum), green and red (maximum) indicates the amplitude of normalized displacements. (b) Comparison between displacements of quasi-plane shear waves (dotted red) and adaptive torsional shear waves (dashed red). The distance of 0 mm corresponds to the center symmetry axis of the circular adaptive torsional shear wavefront corresponding to the center of the hard inclusion. MDM images were normalized to its maximum displacement amplitude at the same depth as the center of the focused push, at a lateral distance of 3.6 mm, which corresponded to the beginning of the propagation of the generated wavefront. The vertical dashed blue line represents the interface between the surrounding medium and the hard inclusion.

adjusted phase delays (dashed red), and with quasi-plane shear waves (dotted red). Relative displacements after propagation on 15 mm were 91% for ATSW generated with phase delays, 58% for ATSW with zero phases, and only 34% for the AUSB quasi-plane shear wave method.
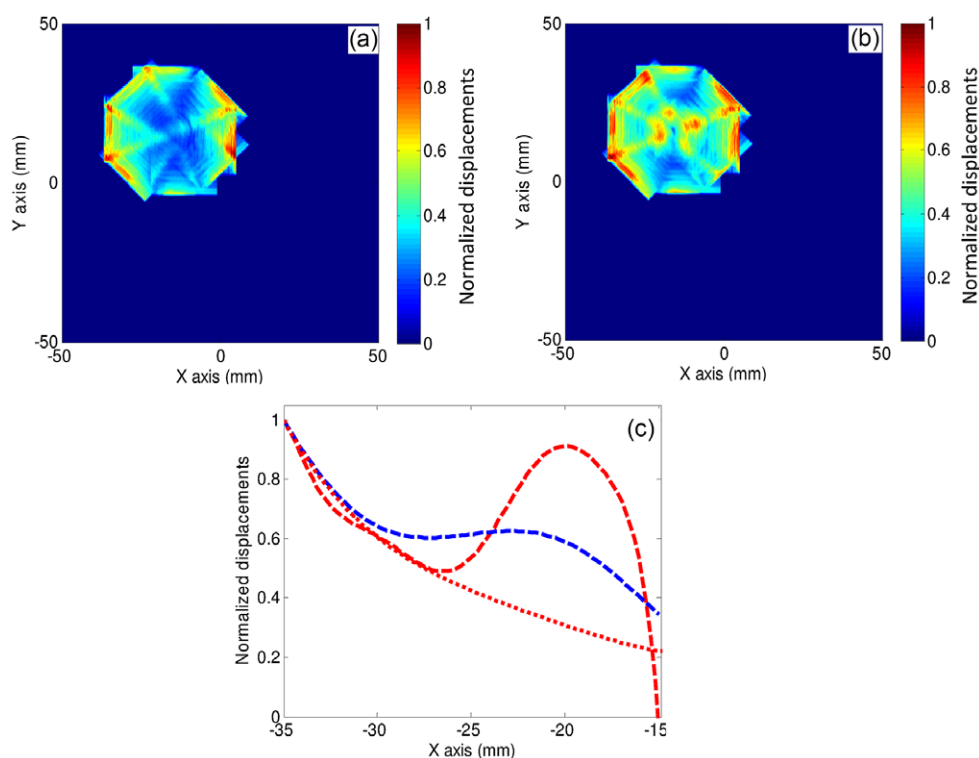
Figure 12. (a) Normalized maximum displacement map of adaptive torsional shear waves generated with zero phases in phantom #6 with $R_{\mathrm{ATSW}} = 20\,\mathrm{mm}$. (b) Normalized maximum displacement map of adaptive torsional shear waves generated with phase delays in phantom #6 with $R_{\mathrm{ATSW}} = 20\,\mathrm{mm}$. In panels (a) and (b), the color scale from blue (minimum), green and red (maximum) indicates the amplitude of normalized displacements. (c) Comparison between displacements of quasi-plane shear waves (dotted red), adaptive torsional shear waves generated with zero phases (dashed-dotted red) and adaptive torsional shear waves generated with phase delays (dashed red). The distance of $-15\,\mathrm{mm}$ corresponds to the center symmetry axis of the circular adaptive torsional shear wavefront. MDM images were normalized to its maximum displacement amplitude at the same depth as the center of the focused push, at a lateral distance of $3.6\,\mathrm{mm}$, which corresponded to the beginning of the propagation of the generated wavefront.

3.4. Signal-to-noise ratios and shear wave velocity measurements

For all phantoms, the SNR of estimated displacements was increased using the adaptive torsional shear wave strategy. For example, in the case of phantom #1, the SNR was increased from 17.5 ± 1.8 dB for quasi-plane shear waves to 26.4 ± 1.2 dB for ATSW with $R_{\mathrm{ATSW}} = 10\,\mathrm{mm}$. For phantoms #2 and #3, the SNR was improved from 17.5 ± 1.4 dB and 16.5 ± 2.2 dB for AUSB to 24.0 ± 1.8 dB and 21.6 ± 2.4 dB for ATSW ($R_{\mathrm{ATSW}} = 10\,\mathrm{mm}$), respectively. In the case of heterogeneous phantoms #4 and #5, the SNR was 4.6 ± 3.4 dB and 3.8 ± 3.6 dB for AUSB, and 14.4 ± 2.5 dB and 9.8 ± 3.6 dB for ATSW, respectively. SNRs were lower in the case of heterogeneous phantoms because measurement ROIs were intentionally located inside inclusions to emphasize benefits of the ATSW method, where displacement magnitudes were lower because of shear wave

Table 2. Signal-to-noise ratio (SNR in dB) of estimated displacements (mean ± standard deviation) generated with adaptive torsional shear waves and quasi-plane shear waves in homogeneous and heterogeneous phantoms. ROIs were defined as a rectangle of 10 mm (axially) by 3 mm (laterally) that was positioned at the same depth as the focus push at lateral distances of 5, 10 and 15 mm (from the push location).

		SNR (dB)		
	Phantom	10 mm	15 mm	20 mm
Adaptive torsional shear waves	Phantom #1	26.4 ± 1.2	14.1 ± 2.4	8.1 ± 3.4
	Phantom #2	24.0 ± 1.8	13.2 ± 2.8	7.4 ± 3.7
	Phantom #3	21.6 ± 2.4	11.5 ± 2.9	6.9 ± 3.7
	Phantom #4	N.A.	14.4 ± 2.5	N.A.
	Phantom #5	N.A.	9.8 ± 3.6	N.A.
Quasi-plane shear waves	Phantom #1	17.5 ± 1.8	9.3 ± 2.6	4.8 ± 3.6
	Phantom #2	17.5 ± 1.4	8.1 ± 3.0	4.7 ± 3.4
	Phantom #3	16.5 ± 2.2	7.9 ± 3.6	3.6 ± 3.4
	Phantom #4	N.A.	4.7 ± 3.4	N.A.
	Phantom #5	N.A.	3.9 ± 3.6	N.A.

Table 3. Shear wave velocity of the quasi-plane shear wave and of the adaptive torsional shear wave ($R_{ATSW} = 20$ mm) methods estimated using the time-of-flight algorithm in two different regions of interest (ROI) of homogeneous phantoms #1, #2 and #3. ROIs were defined as a rectangle of 10 mm (axially) by 5 mm (laterally), located at the same depth as the focused push and at lateral distances (from the push location) of 1 mm for the first ROI and 13 mm for the second one.

		Shear wave velocity (m s^{-1})		
	Phantom	ROI 1	ROI 2	Variation (%)
Adaptive torsional shear waves	Phantom #1	1.38 ± 0.02	1.41 ± 0.02	2.3%
	Phantom #2	2.54 ± 0.03	2.61 ± 0.03	2.7%
	Phantom #3	3.10 ± 0.01	3.18 ± 0.02	2.5%
Quasi-plane shear waves	Phantom #1	1.39 ± 0.02	1.41 ± 0.02	1.9%
	Phantom #2	2.56 ± 0.03	2.69 ± 0.03	5.2%
	Phantom #3	3.07 ± 0.01	3.34 ± 0.03	9%

reflections at the inclusion boundary. SNR assessments were not performed for phantom #6. Detailed results are given in table 2.

The benefit of using the proposed ATSW method is also appreciated from results given in table 3. For homogeneous phantoms #1, #2 and #3 with incremental stiffness increases, the ATSW protocol provided constant variability in shear wave velocities between distant measurement sites (2.3 to 2.7%), whereas AUSB gave higher variability with stiffness (1.9% for phantom #1 with $\mu = 2.1$ kPa to 9.0% for phantom #3 with $\mu = 12.5$ kPa).

3.5. Post processing in the frequency domain and observation of mechanical resonances

As depicted in figure 1, the processing of temporal displacement fields using FFT allowed obtaining stationary displacement maps (SDM) at specific frequencies. Figure 13 presents the experimental displacement spectrum measured at an arbitrary position *M* (white cross) within the soft inclusion of phantom #4. Similar spectra were obtained at other positions within the
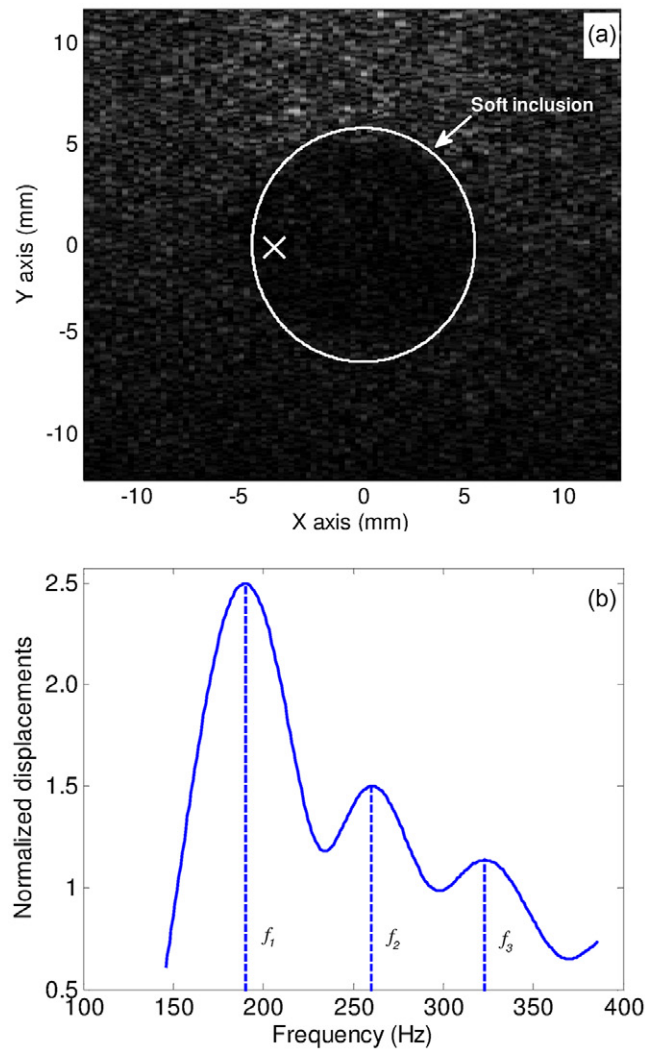
Figure 13. (a) B-mode image of the heterogeneous phantom #4 with a soft inclusion. The white cross within the soft inclusion represents the displacement spectrum measurement site M $(-4, 0\,mm)$. (b) Normalized displacement spectrum within the soft inclusion with respect to the focus push.

inclusion. As noticed, an amplification of displacements is seen at the frequency $f_1 = 190$ Hz; this is typical of a mechanical resonance, as reported earlier (Hadj-Henni *et al* 2010, 2012, Schmitt *et al* 2013). Two other dominant frequencies clearly appeared at $f_2 = 260$ Hz and $f_3 = 324$ Hz. Figure 14(a) shows the stationary displacement field of ATSW at the first resonance frequency (190 Hz) in that phantom #4. Displacements inside the soft inclusion at f_1 were greater than those at focused pushes. This phenomenon is further emphasized in panel (b) reporting maximum displacements of quasi-plane shear waves versus ATSW at f_1. The resonance raised displacements within the inclusion by a factor of 2.5 (dashed red), which further improved displacements when compared to AUSB (dotted red).
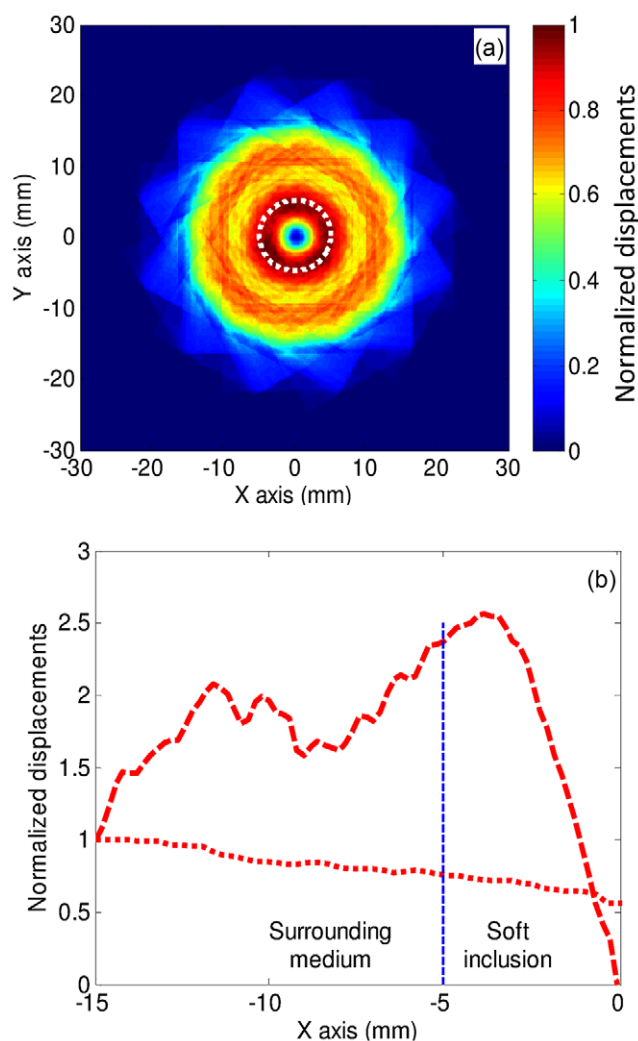
Figure 14. (a) Normalized stationary displacement map (SDM) of adaptive torsional shear waves at the first resonance frequency $f_1 = 190$ Hz generated around the soft inclusion of phantom #4 with $R_{ATSW} = 15$ mm. The white dashed circle represents the position of the soft inclusion. The color scale from blue (minimum), green and red (maximum) indicates the amplitude of normalized displacements. (b) Comparison between displacements of quasi-plane shear waves (dotted red) and adaptive torsional shear waves (dashed red) at the first resonance frequency. The distance at 0 mm corresponds to the center symmetry axis of the circular adaptive torsional shear wavefront corresponding to the center on the soft inclusion. The vertical dashed blue line represents the interface between the surrounding medium and the soft inclusion.

4. Discussion

4.1. Validity of the ATSW reconstruction maps assuming linear superposition of displacements

Figures 7 and 8 allowed appreciating similarities between displacement maps obtained by FEM simulations with or without assuming superposition of quasi-plane wavefronts. The slight

differences between figures 7(b) and (c)—i.e. between the adaptive torsional shear wave pattern assuming linear superposition and that obtained by FEM simulation of simultaneous shear wave sources—are likely due to wave interferences considered by modeling all radiation pressure pushes around the circular path. However, when considering displacements along black arrows of figure 7, those differences were minimized as reflected by reported R^2 of 0.97, mean RE of 0.5% and maximum RE of 11.3% (see figure 8(a)). From this noticing, we could use linear superposition of experimental displacement maps to mimic the concept of the octagonal array probe theoretically introduced in Ekeom *et al* (2013). One can nevertheless observe differences between reconstructed simulated and experimental ATSW patterns, either in 2D when comparing figures 7(b) and (d), or in 1D along black arrows in figure 8(b). These differences are explained by the fact that the viscosity was not taken into account in the simulated data. This means that displacements were less attenuated in the simulation than experimentally.

4.2. Frequency-adapted torsional shear waves and displacement enhancement

It was observed for all phantoms that displacements generated by ATSW were greater than those obtained by the quasi-plane shear wave method (i.e. AUSB with two plane-wave fronts moving in opposite directions—note that the commercialized SSI technique (similar to AUSB) uses more than one line of radiation pressure excitation to reduce the impact of attenuation and to allow shear wave imaging over a wider lateral distance of the image plane). In the current study, the enhancement of displacements using ATSW is attributed to the superposition of constructive interferences of the different quasi-plane shear wavefronts during their inward propagation. For a given radius R_{ATSW}, different enhancements were noticed in figure 9 because each homogeneous phantom had its own mechanical property (see table 1). For example, with $R_{ATSW} = 20$ mm and a propagation distance of 18 mm, relative displacements were at 83% for phantom #1, 66% for phantom #2 and 59% for phantom #3. The ATSW method also allowed improving the signal-to-noise ratio of estimated displacements in all phantoms. It was also shown that the ATSW method provided fair improvements in shear wave velocity measurements for the case of intermediate and stiffest phantoms (phantoms #2 and #3), whereas it gave similar results for the softest phantom #1. The latter comparisons were done between the quasi-plane shear wave and only one wavefront of the adaptive torsional shear wave method, which were thus local comparisons and not global comparisons. Indeed, the total energy transmitted in the medium using ATSW was eight times higher relative to the quasi-plane shear wave strategy, but the energy transmitted locally at each focus push was exactly the same.

It should be noted that in the case of phantoms #1 to #5, all circular ATSW were reconstructed from quasi-plane shear wavefront with a zero-phase at the origin. This was motivated by the circular geometry of the problem (ATSWs generated around a circular path) and by the mechanical property of each phantom being either locally homogeneous or heterogeneous with a center axis symmetry. As proposed by Ekeom *et al* (2013), the octagonal probe design should allow flexible propagation paths around a breast lesion. For example, if one considers a non-symmetrical path (e.g. torsional shear waves generated around an ellipse) or a heterogeneous propagating medium (e.g. phantom #6), the phase needs to be modified by introducing delays between each radiation pressure source to obtain optimum enhancement of tissue displacements. The estimation of phases was implemented by considering two consecutive ATSW excitations, the first one with zero phases to characterize the 2D propagation path and the second one adapted by considering the time reversal principle (Fink 1992). Results could demonstrate that ATSW generated with phase delays enhanced further the amplitude of displacements than ATWS generated with zero phases.

4.3. Shear wave induced resonance phenomenon

As shown in figure 13(b), a mechanical resonance at 190 Hz was observed in the case of the heterogeneous phantom #4 with a soft inclusion. Displacements inside the inclusion were 2.5 times greater than those at the focused push and more than 3.5 times greater than those obtained with the quasi-plane shear wavefront after propagating over the same distance. The observation of a mechanical resonance is in agreement with previous results obtained either by simulations of ATSW (Ekeom *et al* 2013), or by experiments with torsional waves generated mechanically with an oscillating cup applied on the surface of phantoms or on a women breast (Hadj-Henni *et al* 2012). As discussed in Hadj-Henni *et al* (2010, 2012), the resonance spectrum depends on the dimension and geometry of the inclusion, and on the viscoelasticity contrast between the inclusion and the surrounding medium. For example, for a spherical inclusion with a radius of 7.5 mm and a complex shear modulus $G_s = 2700 + 0.054\ i\omega$ Pa embedded in a surrounding homogeneous medium with $G_s = 17600 + 0.7\ i\omega$ Pa, the first resonance frequency was 140 Hz (Hadj-Henni *et al* 2012).

In the present study, no resonance was observed with experiments using quasi-plane shear waves, whereas earlier reports using a vibrating plate to generate plane shear waves allowed observing mechanical resonances (Hadj-Henni *et al* 2010, Schmitt *et al* 2013). This is likely attributed to differences in displacement magnitudes between experiments. Indeed, much higher displacements can be obtained with a vibrating plate compared to an *in situ* radiation pressure. Note that in the current study, no mechanical resonance was observed for the heterogeneous phantom #5 with a stiff inclusion. If resonance would occur, this would be at a higher frequency than 190 Hz. However, this was not observed likely either because not enough torsional shear wave energy could be confined inside the inclusion to generate constructive interferences needed for this phenomenon, or the resonance frequency of the inclusion was not within the frequency range of generated shear waves (Hadj-Henni *et al* 2010).

4.4. Clinical perspective

As introduced in Ekeom *et al* (2013), the ATSW technique targets the early detection of breast lesions in young women or women with dense parenchyma, especially BI-RAD3 and BI-RADS4 lesions (Breast Imaging-Reporting and Data System) (Orel *et al* 1999). Certain specific tumors can be softer than the dense parenchyma at first stages of cancer development due to the small amount of collagen present (Provenzano *et al* 2008). Because enhanced displacements could be obtained with the ATSW method, we expect that it would be feasible inducing mechanical resonance of early stage lesions because of the improved SNR compared to quasi-plane shear waves. Moreover, the amplification of displacements at resonance may help the early diagnosis of small breast lesions difficult to identify on B-mode images.

Mature lesions and some benign masses are stiffer than surrounding breast tissues, but some cancers such as ductal carcinoma *in situ* (DCIS) and some mature fibrocystic diseases are softer than the parenchyma (Krouskop *et al* 1998, Tanter *et al* 2008). For example, according to Krouskop *et al* (1998), the elasticity of the parenchyma is between 28 kPa to 35 kPa, whereas that of DCIS tumors varies from 22 kPa to 26 kPa. In young women, especially in specific ethnic groups such as Asian women, the parenchyma is denser and its elasticity can reach up to 60 kPa (Tanter *et al* 2008, Li 2009). Accordingly, the confinement of torsional shear waves to improve SNR and to produce resonance of some categories of malignant lesions is likely feasible, especially in Asian women. In other ethnic groups, the presence of

resonance could help improving the specificity of dynamic elastography by down grading soft BI-RADS 4 lesions, more likely to be benign. Indeed, it was observed that the parenchyma is stiffer than some benign lesions (Tozaki *et al* 2011).

In this study, all acoustic parameters (I_{SPPA}, I_{SPTA} and MI) of ultrasound sequences used to generate shear waves respected FDA thresholds. For comparison, in an *in vivo* study on breast tissue characterization (Tanter *et al* 2008), the temporal average intensity (I_{SPTA}) was 605 mW cm^{-2} and MI was 1.42, whereas they were $I_{SPTA} = 9.6$ mW cm^{-2} and MI $= 0.27$ in the present study.

5. Conclusion

Dynamic elastography allows the quantification of viscoelastic properties providing additional information to standard B-mode imaging. One of the main problems of commercially available ARFI and SSI remote palpation techniques is the strong attenuation of induced shear waves, which can significantly affect the characterization of biological tissues. In this study, a new method was proposed to enhance displacements generated by radiation force using adaptive torsional shear waves. Experimental results were in good agreement with simulations, and it was shown that ATSW can provide resonance of inclusions, thus further increasing the displacement magnitude and the SNR.

Acknowledgments

Appendix

A.1. Acoustic intensity measures

The spatial peak pulse average intensity (I_{SPPA}) is defined as the value of the pulse-average intensity at the point in the acoustic field where the pulse-average intensity is a maximum (at the focus) (Zhou *et al* 2006, Canney *et al* 2008, Nelson *et al* 2009).

$$I_{SPPA} = \frac{P_0^2}{2\rho c} \tag{A.1}$$

where P_0, ρ and c are the maximum pressure at the focus, the density of the medium and the speed of sound, respectively.

The spatial peak temporal average intensity (I_{SPTA}) is defined as the value of the temporal-average intensity at the point in the acoustic field where the temporal-averaged intensity is a maximum during the pulse duration (Zhou *et al* 2006, Canney *et al* 2008, Nelson *et al* 2009).

$$I_{SPTA} = I_{SPPA} * \Delta t \tag{A.2}$$

where Δt is the push duration.

The mechanical index fixes the energy limit to avoid tissue cavitation. This index is defined as the ratio of the maximum value of negative pressure (in MPa) to the root square of the central frequency (in MHz) (Zhou *et al* 2006, Canney *et al* 2008, Nelson *et al* 2009).

$$\mathrm{MI} = \frac{P}{\sqrt{F_\mathrm{c}}} \tag{A.3}$$

where P is the maximum rarefaction pressure (negative pressure) and F_c the central frequency of the transducer.

A.2. Metrics considered for quantifying the performance of the ATSW method

The relative displacement amplitude (RD) was defined as:

$$\mathrm{RD}(\%) = \frac{A_\mathrm{Loc}}{A_\mathrm{fp}} \times 100 \tag{A.4}$$

where A_Loc and A_fp are displacement amplitudes at the location of interest and at the focused push location, respectively.

The relative error (RE) between two displacement spatial plots was calculated at each spatial position using:

$$\mathrm{RE}(\%) = \left| \frac{A_\mathrm{Simulated} - A_\mathrm{Reconstructed}}{A_\mathrm{Simulated}} \right| \times 100 \tag{A.5}$$

where $A_\mathrm{Simulated}$ and $A_\mathrm{Reconstructed}$ represent simulated and reconstructed displacement amplitudes of the adaptive torsional shear wave method. This latter metric was either averaged along the distance considered or defined as a maximum at a given distance.

References

Acevedo P and Das-Gupta D 2002 The measurement of the spatial average temporal average intensity Isata and ultrasonic power W in composite ultrasonic transducers for medical application *Ultrasonics* **40** 819–21

Barnett S B, Ter Haar G R, Ziskin M C, Rott H-D, Duck F A and Maeda K 2000 International recommendations and guidelines for the safe use of diagnostic ultrasound in medicine *Ultrasound Med. Biol.* **26** 355–66

Bercoff J, Tanter M and Fink M 2004 Supersonic shear imaging: a new technique for soft tissue elasticity mapping *IEEE Trans. Ultrason. Ferroelectr. Freq. Control* **51** 396–409

Calle S, Remenieras J-P, Matar O B, Hachemi M E and Patat F 2005 Temporal analysis of tissue displacement induced by a transient ultrasound radiation force *J. Acoust. Soc. Am.* **118** 2829–40

Canney M S, Bailey M R, Crum L A, Khokhlova V A and Sapozhnikov O A 2008 Acoustic characterization of high intensity focused ultrasound fields: a combined measurement and modeling approach *J. Acoust. Soc. Am.* **124** 2406–20

Chen S *et al* 2013a Assessment of liver viscoelasticity by using shear waves induced by ultrasound radiation force *Radiology* **266** 964–70

Chen X, Shen Y, Zheng Y, Lin H, Guo Y, Zhu Y, Zhang X, Wang T and Chen S 2013b Quantification of liver viscoelasticity with acoustic radiation force: a study of hepatic fibrosis in a rat model *Ultrasound Med. Biol.* **39** 2091–102

Deffieux T, Montaldo G, Tanter M and Fink M 2009 Shear wave spectroscopy for *in vivo* quantification of human soft tissues visco-elasticity *IEEE Trans. Med. Imaging* **28** 313–22

Ekeom D, Hadj-Henni A and Cloutier G 2013 Design of a phased array for the generation of adaptive radiation force along a path surrounding a breast lesion for dynamic ultrasound elastography imaging *IEEE Trans. Ultrason. Ferroelectr. Freq. Control* **60** 552–61

Elkateb Hachemi M, Callé S and Remenieras J P 2006 Transient displacement induced in shear wave elastography: comparison between analytical results and ultrasound measurements *Ultrasonics* **44** e221–5

Fink M 1992 Time reversal of ultrasonic fields. I. Basic principles *IEEE Trans. Ultrason. Ferroelectr. Freq. Control* **39** 555–66

Gennisson J L and Cloutier G 2006 Sol-gel transition in agar-gelatin mixtures studied with transient elastography *IEEE Trans. Ultrason. Ferroelectr. Freq. Control* **53** 716–23

Hadj-Henni A, Schmitt C and Cloutier G 2010 Shear wave induced resonance elastography of soft heterogeneous media *J. Biomech.* **43** 1488–93

Hadj-Henni A, Schmitt C, Trop I and Cloutier G 2012 Shear wave induced resonance elastography of spherical masses with polarized torsional waves *Appl. Phys. Lett.* **100** 133702

Hah Z, Hazard C, Mills B, Barry C, Rubens D and Parker K 2012 Integration of crawling waves in an ultrasound imaging system. Part 2: signal processing and applications *Ultrasound Med. Biol.* **38** 312–23

Hazard C, Hah Z, Rubens D and Parker K 2012 Integration of crawling waves in an ultrasound imaging system. Part 1: system and design considerations *Ultrasound Med. Biol.* **38** 296–311

Krouskop T A, Wheeler T M, Kallel F, Garra B S and Hall T 1998 Elastic moduli of breast and prostate tissues under compression *Ultrason. Imaging* **20** 260–74

Li J 2009 The effects of menstrual cycle, site and individual variation on breast elasticity and thickness *M. Phil. thesis* Department of Health Technology and Informatics, The Hong Kong Polytechnic University

Mamou J and Oelze M L 2013 *Quantitative Ultrasound in Soft Tissues* (Netherlands: Springer) pp 75–9

Montagnon E, Hadj-Henni A, Schmitt C and Cloutier G 2014 Rheological assessment of a polymeric spherical structure using a 3D shear wave scattering model in dynamic spectroscopy elastography *IEEE Trans. Ultrason. Ferroelectr. Freq. Control* **61** 277–87

Montagnon E, Hissoiny S, Despres P and Cloutier G 2012 Real-time processing in dynamic ultrasound elastography: a GPU-based implementation using CUDA *11th Int. Conf. on Information Science, Signal Processing and their Applications (ISSPA)* pp 472–7

Narayana P A and Ophir J 1983 A closed form method for the measurement of attenuation in nonlinearly dispersive media *Ultrason. Imaging* **5** 17–21

Nelson T R, Fowlkes J B, Abramowicz J S and Church C C 2009 Ultrasound biosafety considerations for the practicing sonographer and sonologist *J. Ultrasound Med.* **28** 139–50

Nightingale K, McAleavey S and Trahey G 2003 Shear wave generation using acoustic radiation force: *in vivo* and *ex vivo* results *Ultrasound Med. Biol.* **29** 1715–23

Nightingale K R, Palmeri M L, Nightingale R W and Trahey G E 2001 On the feasibility of remote palpation using acoustic radiation force *J. Acoust. Soc. Am.* **110** 625–34

Nightingale K, Soo M S, Nightingale R and Trahey G 2002 Acoustic radiation force impulse imaging: *in vivo* demonstration of clinical feasibility *Ultrasound Med. Biol.* **28** 227–35

Orel S G, Kay N, Reynolds C and Sullivan D C 1999 BI-RADS categorization as a predictor of malignancy *Radiology* **211** 845–50

Ouared A, Montagnon E, Kazemirad S, Gaboury L, Robidoux A and Cloutier G 2015 Frequency adaptation for enhanced radiation force amplitude in dynamic elastography *IEEE Trans. Ultrason. Ferroelectr. Freq. Control* **62** 1453–66

Palmeri M L, Wang M H, Dahl J J, Frinkley K D and Nightingale K R 2008 Quantifying hepatic shear modulus *in vivo* using acoustic radiation force *Ultrasound Med. Biol.* **34** 546–58

Provenzano P, Inman D, Eliceiri K, Knittel J, Yan L, Rueden C, White J and Keely P 2008 Collagen density promotes mammary tumor initiation and progression *BMC Med.* **6** 11

Rudenko O V, Sarvazyan A P and Emelianov S Y 1996 Acoustic radiation force and streaming induced by focused nonlinear ultrasound in a dissipative medium *J. Acoust. Soc. Am.* **99** 2791–8

Sarvazyan A P, Rudenko O V and Nyborg W L 2010 Biomedical applications of radiation force of ultrasound: historical roots and physical basis *Ultrasound Med. Biol.* **36** 1379–94

Sarvazyan A P, Rudenko O V, Swanson S D, Fowlkes J B and Emelianov S Y 1998 Shear wave elasticity imaging: new ultrasonic technology of medical diagnostics *Ultrasound Med. Biol.* **24** 1419–35

Schmitt. C, Hadj Henni A and Cloutier G 2011 Characterization of blood clot viscoelasticity by dynamic ultrasound elastography and modeling of the rheological behavior *J. Biomech.* **44** 622–9

Schmitt C, Montagnon E, Hadj-Henni A, Shijie Q and Cloutier G 2013 Shear wave induced resonance elastography of venous thrombi: a proof-of-concept *IEEE Trans. Med. Imaging* **32** 565–77

Song P, Heng Z, Manduca A, Urban M W, Greenleaf J F and Shigao C 2012 Comb-push ultrasound shear elastography (CUSE): a novel method for 2D shear elasticity imaging of soft tissues *IEEE Trans. Med. Imaging* **31** 1821–32

Tanter M, Bercoff J, Athanasiou A, Deffieux T, Gennisson J-L, Montaldo G, Muller M, Tardivon A and Fink M 2008 Quantitative assessment of breast lesion viscoelasticity: initial clinical results using supersonic shear imaging *Ultrasound Med. Biol.* **34** 1373–86

Tozaki M, Isobe S and Fukuma E 2011 Preliminary study of ultrasonographic tissue quantification of the breast using the acoustic radiation force impulse (ARFI) technology *Eur. J. Radiol.* **80** 182–7

Zhou Y, Zhai L, Simmons R and Zhong P 2006 Measurement of high intensity focused ultrasound fields by a fiber optic probe hydrophone *J. Acoust. Soc. Am.* **120** 676–85